Influence of grain size distribution on the twinning and annealing characteristics in a AZ80 magnesium alloy.

Tapas Chand, Shubham Nayak

College of Engineering Bhubaneswar, Biju Pattnaik University of Technology, Odisha, India

Abstract

The inhomogeneous grain structure of many wrought magnesium alloys, which are produced by hot forming techniques, results in locally varied grain sizes. This work examined how differences in grain size within a material can affect twinning and annealing behavior. To do this, a rolled magnesium alloy with a bimodal grain structure was pre-compressed and then annealed. The coarse-grain region (CGR) exhibited a greater activation of {10–12} twinning during precompression compared to the fine-grain region (FGR), possibly due to the former's lower twinning stress. The CGR had a larger twinned area, stronger twin texture, fewer twin boundaries, and a weaker grain refinement effect than the FGR. As a result, the twin structure formed in the CGR was clearly different from that in the FGR. Because of its high internal strain energy, the FGR's microstructure changed significantly during the annealing process due to grain growth caused by strain-induced boundary migration, whereas the CGR's microstructure stayed almost unchanged because of its relatively low internal strain energy. Consequently, the annealing process that followed produced a homogenous microstructure and nearly eliminated the microstructural variations between the FGR and CGR brought about by the precompression.

1. Introduction

The severity of environmental problems caused by vehicle carbon dioxide emissions is driving up demands from the social and industrial sectors for vehicles to be lighter. From this angle, wrought magnesium alloys have drawn a lot of interest from the transportation sector due to their mechanical qualities that are better than those of cast magnesium alloys, as well as their lower density and higher specific strength when compared to Al alloys and steels. Rolling, extrusion, and forging are common metal forming techniques used to create wrought magnesium alloys at high temperatures. The nucleation and growth of new grains causes dynamic recrystallization (DRX) and significant microstructure changes in magnesium alloys during hot-forming processes. Rare-earth (RE) element addition has been the subject of numerous studies with the goal of enhancing the formability or strength of wrought magnesium alloys [1-4]. However, because of the significant size mismatch between the atoms of the RE element and Mg, RE elements segregate more strongly to grain boundaries than do Zn and Al, which are important alloying elements in commercial Mg alloys like AZ31, AZ80, and ZK60 [5]. The area fraction of the dynamically recrystallized (DRXed)

grains may decrease as a result of a reduction in grain boundary mobility caused by such segregations of the RE element (i.e., solute drag effect) during hot deformation [5-7].

Additionally, it has been noted that high-strength wrought magnesium alloys can be produced by forming procedures carried out at relatively low temperatures—below 200 °C [8–11]. Even though this kind of low-temperature forming can result in incredibly fine DRXed grains, the DRX behavior during hot forming is significantly suppressed because there is not enough thermal energy available for complete DRX to occur. As a result, the material contains a large number of coarse unDRXed grains in addition to the fine DRXed grains [8,12]. Furthermore, when the initial billet's grain size is large, DRX might not occur throughout the material due to a lack of grain boundaries, which serve as DRX nucleation sites [13, 14]. Similarly, partial DRX results from inadequately imposed strain in rolling or extrusion experiments carried out with low rolling reductions or extrusion ratios [12,15]. This incomplete DRX eventually causes the formation of a partially DRXed microstructure made up of coarse unDRXed grains and fine DRXed grains during hot forming. The wrought magnesium alloys that are produced may have an inhomogeneous DRXed grain structure due to the localized formation of dynamic precipitates, even though DRX occurs throughout the material when the applied strain and thermal energy are sufficient [16–19]. For example, complete DRX occurs during hot extrusion, and the extruded alloy exhibits a fully DRXed grain structure when a commercial AZ91 alloy is extruded at 350 °C with an extrusion ratio of 25 (i.e., when extrusion is performed at a high temperature with a high strain) [16]. The average grain size in the region with many precipitates is small (approximately 4.2 μm) due to the enhanced grain boundary pinning effect, while the average grain size in the region with few precipitates is relatively large (approximately 15.5 μm) due to the easy growth of newly formed DRXed grains. This is because Mg17Al12 precipitates formed during extrusion are distributed locally in the material. Therefore, a variety of metallurgical phenomena that arise inhomogeneously during hot-forming or subsequent heat-treatment processes, such as the occurrence of partial DRX or the local difference in the nucleation and growth behaviors of DRXed grains, can readily lead to a bimodal grain structure in wrought Mg alloys.

Since Mg has only two independent basal slip systems at room temperature due to the high critical resolved shear stresses of the non-basal slip systems, it is well known that {10–12} twinning is important to the material's plastic deformation behavior [20–22]. Due to the rearrangement of grain orientations during hot forming, wrought magnesium alloys typically have a strong basal texture. The majority of grains' basal planes are oriented parallel to the processing directions, such as the extrusion direction and rolling direction (RD). Consequently, under compression along the processing directions, {10-12} twinning with a c-axis extension mode is readily activated in wrought magnesium alloys. Numerous perspectives have been taken into consideration when analyzing the {10-12} twinning behavior of wrought magnesium alloys during deformation. These include the tolerance of plastic deformation [23–25], grain refinement brought about by twin boundaries [26,27], textural variation brought about by twinning-induced lattice rotation [28–30], variations in the activation of slip systems brought about by twinning [23,26,30,31], kind and quantity of active twin variants [23,32], and formation of voids and cracks at twins [33]. The

microstructural alterations in wrought magnesium alloys during heat treatment with the goal of altering their texture or enhancing their strength have also been the subject of numerous investigations [34–40]. But rarely have studies taken into account an inhomogeneous grain structure when examining the {10-12} twinning behavior of wrought magnesium alloys with a bimodal structure during compressive deformation and their microstructural evolution during subsequent annealing [41,42]. In order to better understand how a bimodal structure of both coarse and relatively fine DRXed grains affects twinning and annealing behaviors, the current study systematically examines changes in the microstructural and textural characteristics of a rolled AZ31 alloy during its deformation along the direction favorable for {10-12} twinning and its subsequent annealing treatment. Specifically, the study focuses on the impact of the material's variation in grain size.

2. Experimental Procedure

In this study, a 20 mm thick commercial hot-rolled AZ31 Mg alloy (Mg-3Al-1Zn-0.5Mn, wt%) was utilized. It underwent a 10-hour heat treatment at 400 °C to achieve homogenization. A rectangular bar measuring 60 mm in length, 30 mm in width, and 20 mm in thickness, which represent the RD, TD, and ND, respectively, was machined from the homogenized material for precompression. Using an Instron 8516 testing machine, this machined bar was compressed to a plastic strain of 6.0% along the RD at a strain rate of 10^{-3} s^{-1} at room temperature in order to introduce {10-12} twins in the material. Following precompression, the annealing process was carried out in a box furnace that had been preheated for one hour at 250 °C.

Using optical microscopy (OM) and electron backscatter diffraction (EBSD), the microstructure and texture of the as-rolled material were examined, respectively. The OM sample was mechanically polished using abrasive papers ranging from 180 to 2400 grit and 3- and 1-micron diamond pastes. Following this, it was etched using an acetic-picral solution consisting of 3.0 g picric acid, 10 ml acetic acid, 10 ml distilled water, and 100 ml ethanol. The EBSD sample was similarly polished as the OM sample using abrasive papers and diamond pastes; however, to eliminate any strains and produce a superior surface finish, the EBSD sample was further polished for 30 minutes using colloidal silica.

At the same location on the precompressed sample before and after annealing, in situ EBSD measurements were carried out in order to thoroughly examine the microstructural changes of the twin structure. To achieve this, the EBSD sample, measuring 15 mm in length, 15 mm in width, and 4 mm in thickness, was machined into the center of the precompressed bar. Following the previously outlined steps, the sample was polished. A Hitachi SU-70 field-emission scanning electron microscope was then used to measure the EBSD in a 550 x 600 μm^2 scanning area at a step size of 1.0 µm. This sample underwent EBSD measurement, annealing, and a light polish using only colloidal silica to get rid of the surface oxide layer that had formed. The EBSD measurement was then repeated with the same step size and at the same location within the same scanning area. The EBSD data was analyzed using the Tex-SEM Laboratories orientation imaging microscopy (TSL OIM) analysis 7.0 software. To

guarantee the reliability of the analysis results, only data points with large confidence index values—larger than 0.1—were used.

3. Results and discussions

3.1. Microstructural Evolution

Fig. 1(a) displays the optical microstructure and (0001) pole figure of the as-rolled AZ31 alloy. With a maximum intensity of 14.2, the alloy exhibits a strong basal texture, with the majority of the grain basal poles aligned parallel to the ND. With an average grain size of 44.3 μm, the alloy displays a fully DRXed grain structure made up of both relatively fine and coarse DRXed grains. The microstructural changes caused by precompression and subsequent annealing were observed in an area that included both the fine-grain region (FGR) and the coarse-grain region (CGR), as shown in Fig. 1(b), in order to analyze the twinning and annealing behaviors in the bimodal grain structure. The FGR and CGR have average grain sizes of 30.2 μm and 54.8 μm, respectively. A number of deformation twins are formed as a result of the precompression, according to the inverse pole figure map that was created from this particular area (Fig. 1(c)). During compression along the RD, {10-12} extension twinning easily happens because rolled magnesium alloys with an ND basal texture are in the c-axis extension stress state under compressive deformation along directions parallel to the rolling plane. Additionally, in the precompressed material, the RD-oriented twin texture forms newly and the ND-oriented matrix texture is weakened due to the {10-12} twinning, which causes a lattice reorientation of 86.3° on the twinning plane [21] (Fig. 1(c)). The residual matrix region and the twinned region in the FGR and CGR following precompression are displayed in Fig. 2. In the CGR, the area fraction of the twinned region is 75.5%, whereas in the FGR, it is 66.3%. While many grains in the CGR are nearly entirely twinned and have twin bands covering their whole surface, the majority of grains in the FGR are only partially twinned and have multiple parallel twin bands formed within a grain (Fig. 2(a) and (c)). Due to the formation of twin bands, the average grain size decreases in both the FGR and CGR due to precompression (from 30.2 μm to 20.2 μm in the FGR and from 54.8

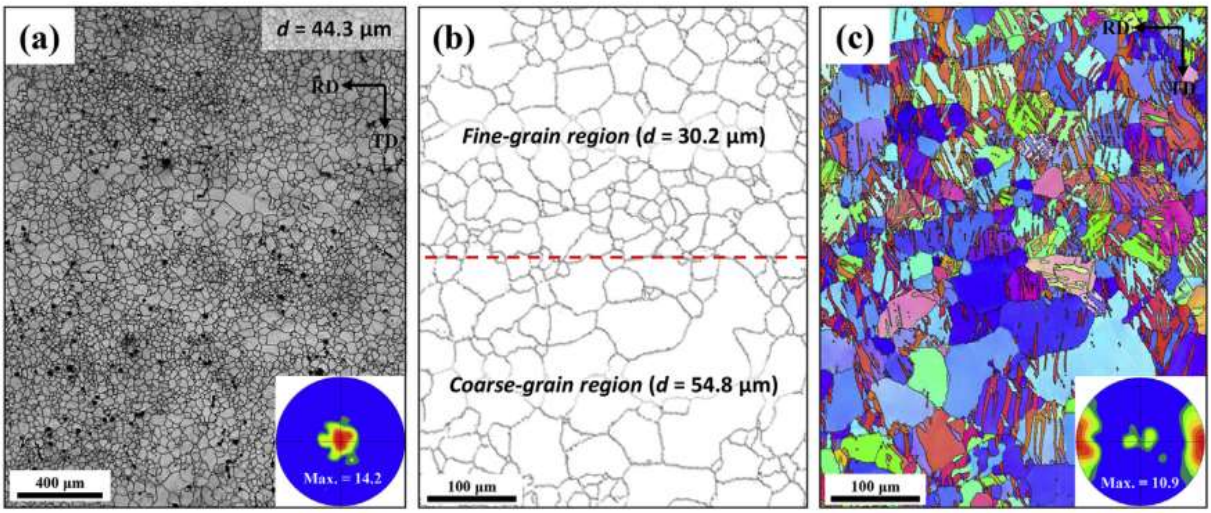

μm to 40.7 μm in the CGR).

Fig. 1. a) Optical micrograph and (0001) pole figure of as-rolled material, (b) high-angle grain boundary map of area consisting of fine-grain region and coarse-grain region, and (c) inverse pole figure map and (0001) pole figure of area in (b) after precompression. d denotes the average grain size.

3.2. Variations in twin structures of FGR and CGR with annealing

The precompressed FGR and CGR, respectively, in situ EBSD observation results are shown in Figs. 3 and 4, before and after annealing. With annealing, the FGR's microstructure changes significantly (Fig. 3). The original grain morphology and twin boundaries disappear as some of the twinned and residual matrix regions grow and encroach on the surrounding area, resulting in the formation of relatively coarse new grains with few twins (Fig. 3(b)). As a result, the length of {10-12} twin boundaries drastically reduces from 29.9 mm to 9.8 mm, while the average grain size rises from 20.2 μm to 34.1 μm. On the other hand, the finely recrystallized grains that are newly formed at the twin boundaries and grain boundaries during annealing are responsible for the lengthening of high-angle grain boundaries (HAGBs) from 15.1 mm to 22.8 mm (Fig. 3). Furthermore, following precompression, the maximum texture intensity of the FGR rises from 9.9 to 11.6 due to the twinned region's more noticeable growth behavior than the residual matrix region's. On the other hand, annealing does not significantly alter the microstructure of the CGR (Fig. 4). The original grain structure and twin bands are largely preserved in the CGR because the twinned and residual matrix regions only slightly expand. However, because the fine recrystallized grains that form in the FGR are easily consumed by the growth of other coarse grains around them, the number of fine recrystallized grains is higher in the CGR than in the FGR. As a result, there are comparatively few recrystallized grains in the FGR, where the growth of residual grains and twin bands happens actively. As a result of the CGR's suppressed growth behavior, many fine recrystallized grains are present, which ultimately causes the average grain size to slightly decrease from 40.7 μm to 39.2 μm. This decrease in CGR grain size as a result of annealing is in contrast to the FGR's increase in grain size. The CGR's suppressed growth behavior and the FGR's promoted growth behavior can also be attributed to these differences. The maximum texture intensity change for the CGR likewise exhibits a trend that differs from the FGR's; following annealing, the FGR's texture intensity increases by 17.2%, from

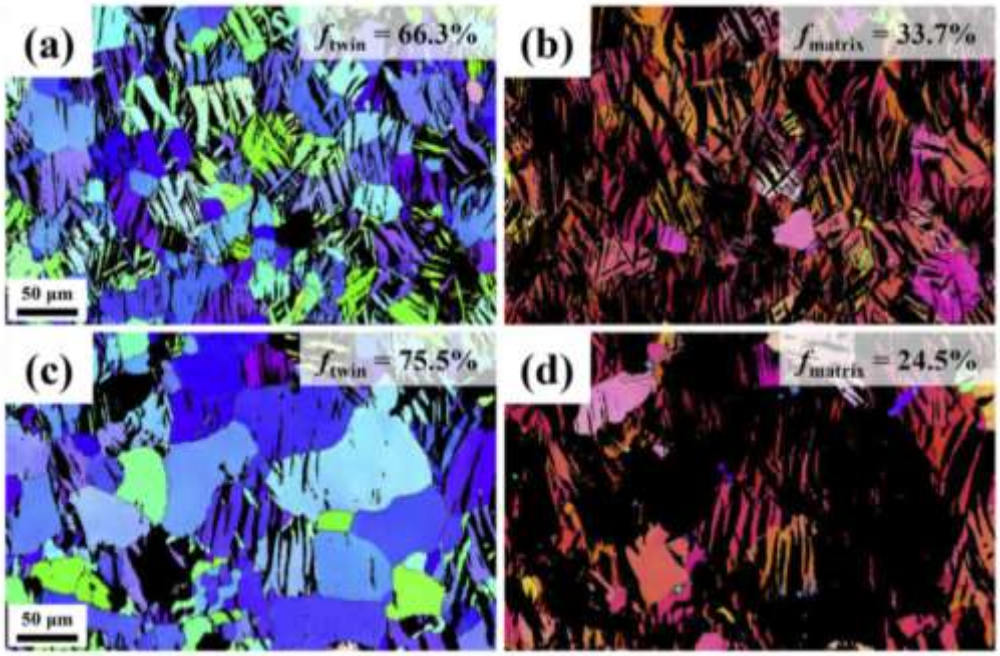

9.9 to 11.6, while the CGR's texture intensity decreases by

Fig. 2. Inverse pole figure maps of (a, c) twinned region and (b, d) residual matrix region of (a, b) fine-grain region and (c, d) coarse-grain region after precompression. f_{twin} and f_{matrix} denote the area fractions of the twinned region and residual matrix region, respectively.

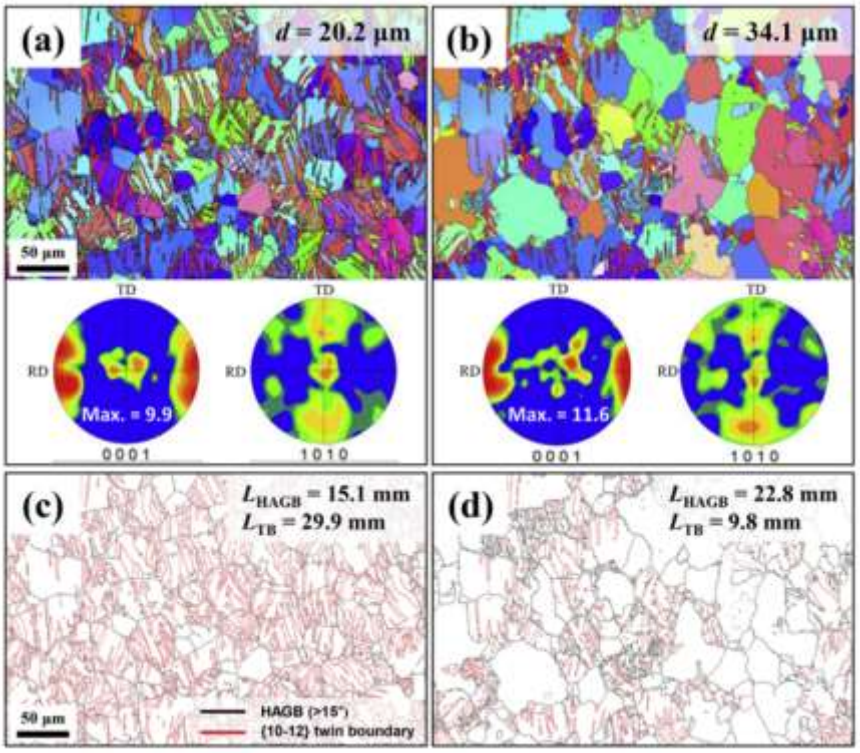

Fig. 3. In situ EBSD results showing microstructural changes in fine-grain region with subsequent annealing: (a, b) inverse pole figure maps and (0001) and (10-10) pole figures and (c, d) grain and twin boundary maps (a, c) before and (b, d) after annealing. d denotes the average grain size. LHAGB and LTB denote the lengths of high-angle grain boundaries and {10-12} twin boundaries, respectively.

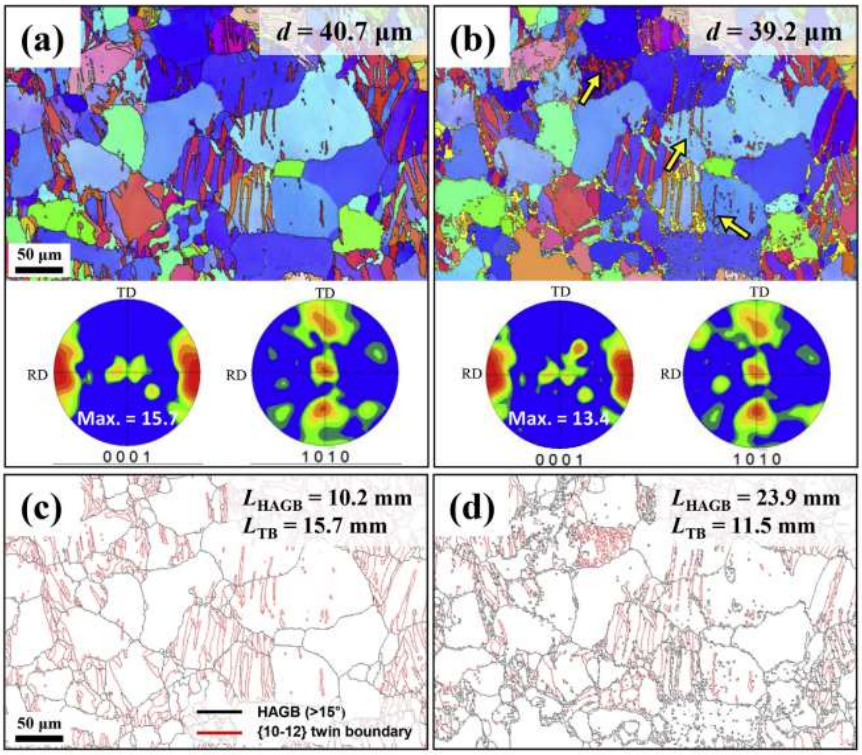

Fig. 4. In situ EBSD results showing microstructural changes in coarse-grain region with subsequent annealing: (a, b) inverse pole figure maps and (0001) and (10-10) pole figures and (c, d) grain and twin boundary maps (a, c) before and (b, d) after annealing. d denotes the average grain size. LHAGB and LTB denote the lengths of high-angle grain boundaries and {10-12} twin boundaries, respectively

14.6%, from 15.7 to 13.4. Due to the formation of numerous recrystallized grains with comparatively random orientations and the occurrence of detwinning of the initial twin bands (see the yellow arrows in Fig. 4(b)), the RD-oriented twin texture is weak, which causes the intensity reduction of the CGR.

3.3. Variations in twinning behavior with grain size difference

The bimodal structure of the rolled magnesium alloy causes the initial grain size difference between the FGR and CGR, which in turn causes notable variations in the twinning behaviors of these regions during precompression. Generally, the Hall–Petch equation, $\sigma = \sigma_0 + kd^{-1/2}$, which denotes the yield strength, friction stress, Hall–Petch coefficient, and average grain size, respectively, describes how the activation of deformation mechanisms in polycrystalline metal materials depends on grain size [21]. The activation stresses for twinning and slip increase with a decrease in grain size because both twinning and dislocation slip obey the Hall-Petch law. On the other hand, twinning is known to be more susceptible to grain size than dislocation slip [43–45]. In fact, the k value in an extruded AZ31 alloy, which relates to the slope of the Hall—Petch equation, is 1.58 times greater than that of dislocation slip under tension along the extrusion direction (282 MPa μm−1/2 for twinning and slip, respectively) [43]. This is true for {10–12} twinning under compression along the extrusion direction. $\Delta\sigma_{twinning}=k\cdot(d_{FGR}^{-1/2}-d_{CGR}^{-1/2})$, where d_{FGR} and d_{CGR} are the initial grain sizes of the FGR and CGR, respectively, can be used to express the difference in the twinning stress, $\Delta\sigma_{twinning}$, caused by the difference in the initial grain sizes of the FGR and CGR. The calculated value of $\Delta\sigma_{twinning}$ was approximately 13.2 MPa. The difference between the twinning stresses in the FGR and CGR is represented by the $\Delta\sigma_{twinning}$ value (13.2 MPa), which is approximately 21% of the compressive yield strength of the as-rolled material made up of the FGR and CGR (61.4 MPa). As a consequence, there is a notable variation in the activation of {10-12} twinning in these two regions during compression due to the differences in the grain sizes of the FGR and CGR. Therefore, the area fraction of the {10-12} twins formed at the same applied compressive stress is larger in the CGR (75.5%) than in the FGR (66.3%) due to the easier activation of {10-12} twinning in the larger grain size of the CGR. This also results in a higher texture intensity of the CGR due to its stronger RD-oriented twin texture.

Additionally, because multiple twin bands form within a single grain, many twin boundaries are formed in the grains in the FGR. As a result, the twin bands effectively divide the grains, significantly lowering the average grain size. On the other hand, because the formed twin bands merge with one another to occupy the entire grain, the CGR has comparatively fewer twin boundaries. As a result, the FGR's (refinement of ~33%, from 30.2 μm to 20.2 μm) and the CGR's (refinement of ~26%, from 54.8 μm to 40.7 μm) grain refinement effect caused by twin boundaries is smaller.

As a result, compared to the FGR, which has finer grains, the CGR's coarser grains facilitate the {10–12} twinning behavior during precompression to a greater extent. This results in the formation of a larger twinned region, a higher texture intensity, fewer twin boundaries, and a weaker grain refinement effect after precompression.

3.4. Variations in annealing behavior with grain size difference

The growth of the twinned and residual matrix regions is the primary cause of the variation in the microstructure of the precompressed material during annealing, as explained in section 3.2. Twin boundaries and grain boundaries migrate via atomic diffusion at both types of boundaries, which leads to the growth of twin bands and grains. While the suppressed migration of the boundaries in the CGR results in almost no changes in the microstructure even after annealing, the promoted migration of the boundaries in the FGR during the annealing treatment of the precompressed material causes a drastic change in the microstructure (Fig. 3). The presence of multiple driving forces, including the grain boundary energy, stored strain energy, surface energy, chemical driving force, magnetic field, elastic energy, and temperature gradient, is known to cause boundary migration in materials [46]. In polycrystalline bulk metallic materials, the dominant driving forces are the grain boundary energy and stored strain energy. Fully homogenized metals have relatively low stored strain energy because the homogenization treatment eliminates a significant portion of the material's dislocations through dislocation climb and cross-slip. Boundary migration takes place in these low-stored-strain energy materials to lower the area fraction of grain boundaries, which are two-dimensional lattice defects with a high surface energy [47]. However, in deformed materials, boundary migration occurs in order to reduce the internal strain energy stored in the grains—rather than the grain boundaries themselves—- because numerous dislocations are formed and tangled within the grains by the activation of multiple dislocation slips during plastic deformation. Therefore, the driving force for boundary migration in plastically deformed materials is the internal strain energy [48,49], and the phenomenon of boundary migration caused by internal strain energy as the driving force is well-known as strain-induced boundary migration (SIBM) [50–52]. The driving force for SIBM (P) is proportional to the dislocation density, i.e., $P = (\rho\mu b2)/2$, where ρ, μ, and b are the dislocation density, shear modulus, and Burgers vector, respectively, because the internal strain energy is strongly correlated with the number of residual dislocations in a material [46]. For this reason, the density of the dislocations created by the application of compressive deformation determines the internal strain energy of the precompressed material in this investigation prior to annealing.

Dislocation slip always occurs in conjunction with twinning; deformation cannot be accommodated by twinning alone, even in cases where the external stress applied to a material is entirely favorable for {10–12} twinning [47]. Dislocation slip is triggered in addition to {10-12} twinning, which is the predominant deformation mechanism during precompression along the RD as conducted in this study. The area fraction of the twinned region, the average Schmidt factor (SF) for {10-12} twinning under deformation conditions, the shear of {10-12} twinning, and the strain accommodated by {10-12} twinning can all be found by using the formula $\varepsilon_{twin} = f_{twin} \cdot \bar{m} \cdot \gamma_{twin}$ [20]. According to EBSD analysis, the average SF for {10-12} twinning of the as-rolled material under compression along the RD is 0.40. The area fractions of the twinned regions of the FGR and CGR are 66.3% and 75.5%,

respectively. Given that the {10-12} twinning shear in magnesium is 0.129 [53], the FGR and CGR's computed twinning strains are 3.42% and 3.90%, correspondingly. By deducting the twinning strain from the applied plastic strain (6.0%), it is simple to calculate the strain accommodated by dislocation slip, also known as slip strain. The FGR and CGR have slip strains of 2.58% and 2.10%, respectively. Consequently, the dislocation slip accommodates 43% of the total deformation in the FGR and 35% of the total deformation in the CGR. More dislocations form during precompression in the FGR due to a stronger activation of slip in the FGR compared to the CGR. The quantity of low-angle grain boundaries (LAGBs), which is correlated with the material's dislocation density, can support this. The length of the LAGBs after precompression in the FGR (9.06 mm) is significantly longer than that in the CGR (4.27 mm) in areas of equal size (Fig. 5(a) and (d)). Furthermore, the kernel average misorientation (KAM) and grain orientation spread (GOS) values acquired from EBSD measurements can be used to express the internal residual strain of a material [54]. To describe the local misorientation at specific measurement points and within each grain, respectively, KAM and GOS analyses have been applied extensively [54, 55]. Fig. 5 displays the KAM and GOS maps of the FGR and CGR following precompression. These maps show that the FGR has higher average KAM and GOS values than the CGR. These findings suggest that the precompression in the FGR produces a higher internal strain energy than in the CGR, which means that microstructural changes happen more severely in the FGR during subsequent annealing. SIBM takes place during heat treatment of deformed materials in order to reduce the material's overall strain energy; as a result, the low internal strain energy regions expand toward the higher strain energy adjacent regions [52]. This behavior is evident in the FGR, where the annealing-related microstructural evolution is significantly more prominent than in the CGR. During annealing (Fig. 6(a),(b)), the growth of two grains, B and C (represented by the yellow circles in Fig. 6(a)) adjacent to grain A, completely consumes grain A, which is represented by the red circle in the FGR. Grain A has a higher internal strain energy than grains B and C, according to the KAM map of the FGR prior to annealing (Fig. 6(c)). This suggests that the difference in dislocation densities on the opposing sides of the boundary is what causes the boundary migration, which in turn causes the boundary to shift from a region with a high dislocation density to one with a lower dislocation density, reducing the material's total strain energy.

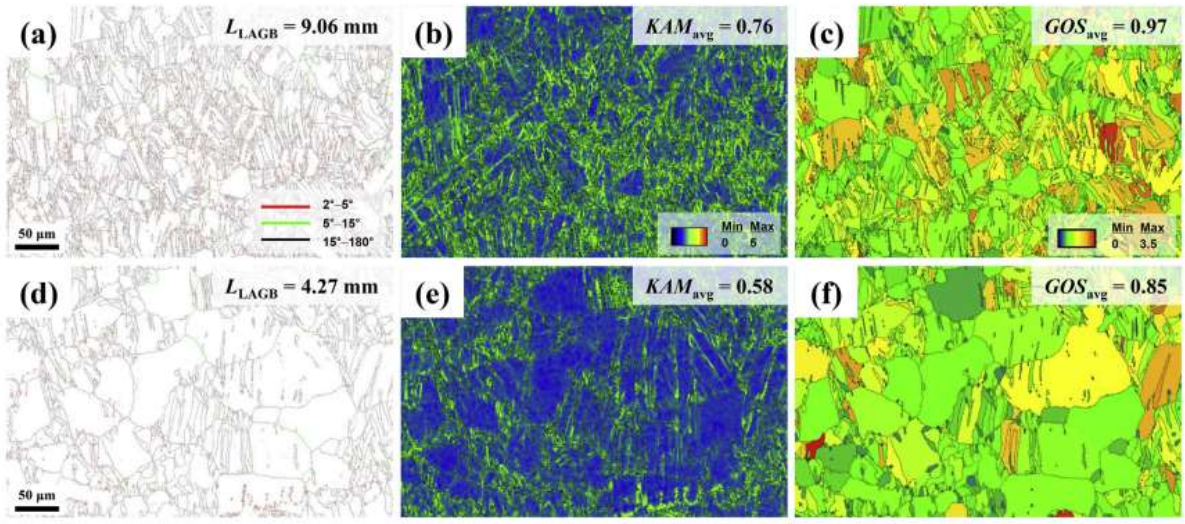

Fig. 5. EBSD results showing difference in internal strain between (a–c) fine-grain region and (d–f) coarse-grain region after precompression: (a, d) grain boundary maps, (b, e) kernel average misorientation (KAM) maps, and (c, f) grain orientation spread (GOS) maps. LLAGB, KAMavg, and GOSavg denote the length of low-angle grain boundaries, average KAM value, and average GOS value, respectively.

3.5. Variations in microstructural differences with precompression and annealing

The grain boundary, KAM, and GOS maps of the annealed FGR and CGR are displayed in Fig. 7. The annealing treatment causes a significant decrease in the LAGB length, KAM value, and GOS value of the FGR; in particular, the LAGBs and internal strain nearly vanish in grains where growth occurs (Fig. 7(a)–(c)). This indicates that the growth of the twinned and residual matrix regions dissipates the strain energy that was accumulated in the FGR as a result of precompression. On the other hand, as shown in Figures 7(e), (f); the decrease in the KAM and GOS values of the CGR due to the annealing treatment is significantly less than that of the FGR. Due to the formation of multiple recrystallized grains, the LAGB length in the CGR even slightly increases from 4.27 mm to 4.69 mm (Fig. 7(d)). One important finding is that the LAGB length, KAM value, and GOS value for the FGR and CGR differ significantly in the precompressed state (Fig. 5). Nevertheless, in the annealed state, these variations significantly diminish or vanish (Fig. 7). These values, which are associated with internal dislocations and strain, also exhibit a tendency in the misorientation angle distribution. Because the FGR has more {10–12} twin boundaries and twin intersections than the CGR, the peaks at 80–90° and 55–60° in the precompressed state are significantly higher in the FGR (Fig. 8(a)). But in the annealed state, there is a significant reduction in the misorientation angle distribution gap between the FGR and the CGR, primarily because there are fewer twin boundaries in the FGR (Fig. 8(b)).

Fig. 9 illustrates the microstructural properties of the FGR and CGR in the precompressed and subsequent annealed states, along with the relative differences between these microstructural properties. All the measured microstructural features (average grain size, maximum texture intensity, lengths of {10-12} twin boundaries, HAGBs, and LAGBs, and average KAM and GOS values) exhibit notable differences (14.1–112.2%) in the precompressed state (Fig. 9). This suggests that the subsequent annealing significantly lessens the significant microstructural differences between the FGR and CGR, which were caused by precompression. Based on these findings, it was determined that when plastic deformation conducive to {10-12} twinning is applied, a variation in grain size at microscopic positions in magnesium alloys with an inhomogeneous grain size distribution can result in the formation of a twin structure with significantly different microstructural characteristics at each position. Nevertheless, a subsequent annealing process can eliminate these microstructural variations, significantly enhancing the material's overall microstructural

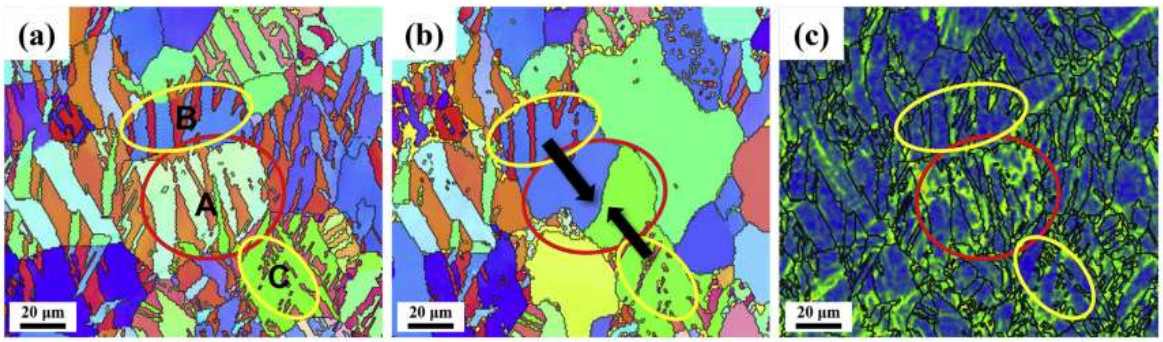

homogeneity.

Fig. 6. In situ EBSD observation results showing growth-dominant microstructural evolution in fine-grained region during annealing: inverse pole figure maps (a) before and (b) after annealing and (c) KAM map before annealing. The yellow and red circles represent regions with low internal strain energy and relatively higher internal strain energy, respectively, before annealing.

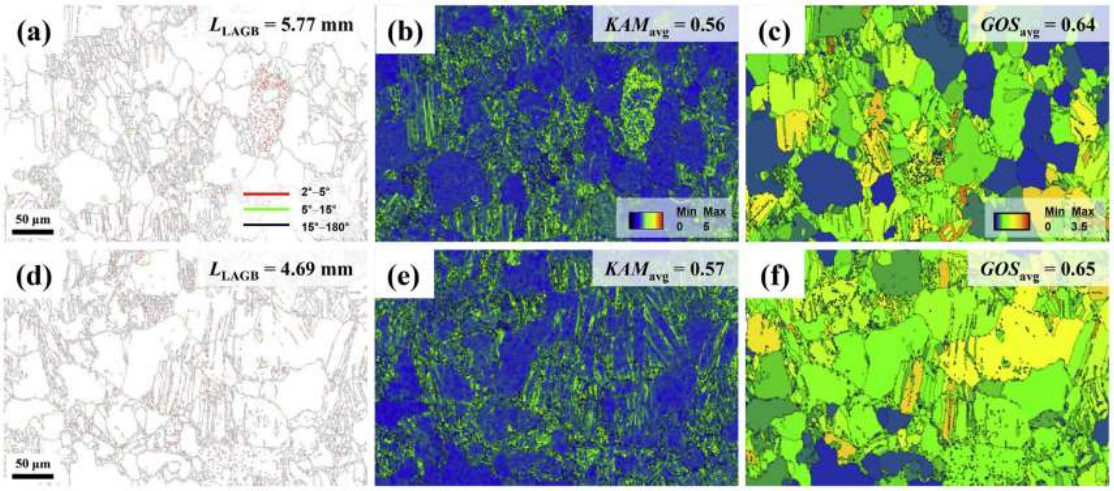

Fig. 7. EBSD results showing difference in internal strain between (a–c) fine-grain region and (d–f) coarse-grain region after subsequent annealing: (a, d) grain boundary maps, (b, e) kernel average misorientation (KAM) maps, and (c, f) grain orientation spread (GOS) maps. LLAGB, KAM_{avg}, and GOS_{avg} denote the length of low-angle grain boundaries, average KAM value, and average GOS value, respectively.

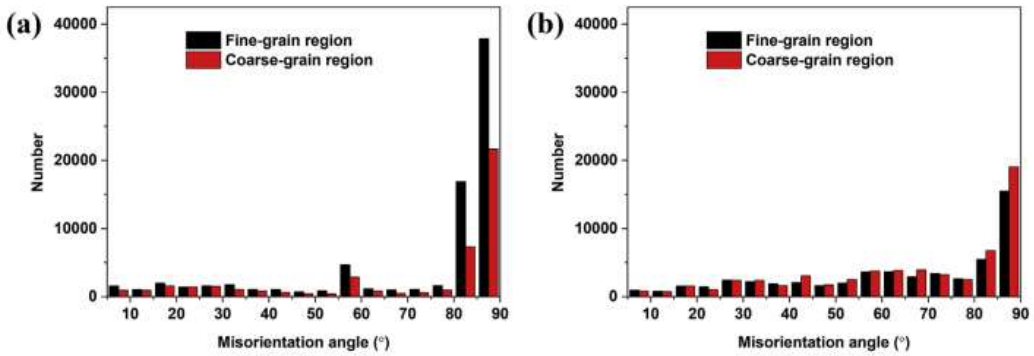

Fig. 8. Misorientation angle distributions in fine- and coarse-grain regions after (a) precompression and (b) subsequent annealing.

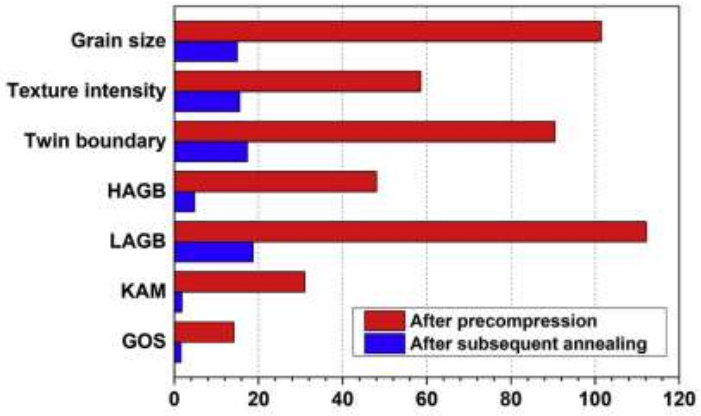

Fig. 9. Differences in microstructural characteristics between fine-grain region and coarse-grain region after precompression and subsequent annealing. Grain size, texture intensity, twin boundary, HAGB, LAGB, KAM, and GOS denote the effective grain size with consideration of twin boundaries, maximum texture intensity of the (0001) pole figure, length of {10-12} twin boundaries, length of

high-angle grain boundaries (> 15°), length of low-angle grain boundaries (2–15°), average KAM value, and average GOS value, respectively

4. Conclusion

The twinning behavior of a rolled magnesium alloy with a bimodal grain structure during precompression and the microstructural changes during the annealing process that followed are examined in this work. The activation of {10-12} twinning and dislocation slip during precompression are found to be significantly influenced by the grain size difference within the material, leading to notable variations in the microstructural properties of the FGR and CGR. Because of the coarser grain size of the CGR, which results in lower twinning stress, the {10–12} twinning behavior is more noticeable in the CGR than in the FGR. Consequently, compared to the precompressed FGR, the precompressed CGR has a higher twin fraction, a stronger texture intensity, fewer twin boundaries, and coarser grains.

References

[1] S. Yi, J. Bohlen, F. Heinemann, D. Letzig, Acta Mater. 58 (2010) 592–605.
[2] J. Bohlen, M.R. Nürnberg, J.W. Senn, D. Letzig, S.R. Agnew, Acta Mater. 55 (2007) 2101–2112.
[3] D. Griffiths, Mater. Sci. Technol. 31 (2015) 10–24.
[4] I.H. Jung, M. Sanjari, J. Kim, S. Yue, Scripta Mater. 102 (2015) 1–6.
[5] J.D. Robson, Metall. Mater. Trans. A 45A (2014) 3205–3212.
[6] M. Bugnet, A. Kula, M. Niewczas, G.A. Botton, Acta Mater. 79 (2014) 66–73.
[7] N. Stanford, G. Sha, J.H. Xia, S.P. Ringer, M.R. Barnett, Scripta Mater. 65 (2011) 919–921.
[8] H. Yu, S.H. Park, B.S. You, Mater. Sci. Eng. A 610 (2014) 445–449.
[9] Y. Go, S.M. Jo, S.H. Park, H.S. Kim, B.S. You, Y.M. Kim, J. Alloy. Comp. 739 (2018) 69–76.
[10] M. Shahzad, L. Wagner, Mater. Sci. Eng. A 506 (2009) 141–147.
[11] Y. Chino, M. Mabuchi, Adv. Eng. Mater. 3 (2001) 981–983.
[12] S.H. Park, B.S. You, R.K. Mishra, A.K. Sachdev, Mater. Sci. Eng. A 598 (2014) 396–406.
[13] M.R. Barnett, A.G. Beer, D. Atwell, A. Oudin, Scripta Mater. 51 (2004) 19–24.
[14] S.H. Park, J.H. Bae, S.H. Kim, J. Yoon, B.S. You, Metall. Mater. Trans. A 46A (2015) 5482–5488.
[15] M. Hirano, M. Yamasaki, K. Hagihara, K. Higashida, Y. Kawamura, Mater. Trans. JIM 51 (2010) 1640–1647.
[16] S.H. Kim, J.U. Lee, Y.J. Kim, B.G. Moon, B.S. You, H.S. Kim, S.H. Park, Mater. Sci. Eng. A 703 (2017) 1–8.
[17] S.W. Bae, S.H. Kim, J.U. Lee, W.K. Jo, W.H. Hong, W. Kim, S.H. Park, J. Alloy. Comp. 766 (2018) 748–758.
[18] S.H. Park, S.H. Kim, Y.M. Kim, B.S. You, J. Alloy. Comp. 646 (2015) 932–936.

[19] S.H. Park, S.H. Kim, H.S. Kim, J. Yoon, B.S. You, J. Alloy. Comp. 667 (2016) 170–177.
[20] C.S. Roberts, Magnesium and its Alloys, John Wiley & Sons, Inc., New York, 1960.
[21] R.E. Reed-Hill, R. Abbaschian, Physical Metallurgy Principles, third ed., PWS-Kent, Boston, 1994.
[22] X.Y. Lou, M. Li, R.K. Boger, S.R. Agnew, R.H. Wagoner, Int. J. Plast. 23 (2007) 44–86.
[23] S.G. Hong, S.H. Park, C.S. Lee, Acta Mater. 58 (2010) 5873–5885.
[24] A. Ishii, J. Li, S. Ogata, Int. J. Plast. 82 (2016) 32–43.
[25] S.H. Park, S.G. Hong, C.S. Lee, Mater. Sci. Eng. A 570 (2013) 149–163.
[26] S.H. Park, S.G. Hong, J.H. Lee, C.S. Lee, Mater. Sci. Eng. A 532 (2012) 401–406.
[27] Y. Xin, M. Wang, Z. Zeng, M. Nie, Q. Liu, Scripta Mater. 66 (2012) 25–28.
[28] S.H. Choi, E.J. Shin, B.S. Seong, Acta Mater. 55 (2007) 4181–4192.
[29] J. Jiang, A. Godfrey, W. Liu, Q. Liu, Scripta Mater. 58 (2008) 122–125.
[30] Y.N. Wang, J.C. Huang, Acta Mater. 55 (2007) 897–905.
[31] L. Jiang, J.J. Jonas, A.A. Luo, A.K. Sachdev, S. Godet, Mater. Sci. Eng. A 445–446 (2007) 302–309.
[32] S.H. Park, S.G. Hong, C.S. Lee, Scripta Mater. 62 (2010) 202–205.
[33] D.K. Xu, E.H. Han, Scripta Mater. 69 (2013) 702–705.
[34] T. Nakata, T. Mezaki, R. Ajima, C. Xu, K. Oh-Ishi, K. Shimizu, S. Hanaki, T.T. Sasaki, K. Hono, S. Kamado, Scripta Mater. 101 (2015) 28–31.
[35] L.W.F. Mackenzie, M.O. Pekguleryuz, Scripta Mater. 59 (2008) 665–668.
[36] Z.R. Zeng, Y.M. Zhu, S.W. Xu, M.Z. Bian, C.H.J. Davies, N. Birbilis, J.F. Nie, Acta Mater. 105 (2016) 479–494.
[37] H.Y. Chao, H.F. Sun, W.Z. Chen, E.D. Wang, Mater. Char. 62 (2011) 312–320.
[38] M. Kohzu, K. Kii, Y. Nagata, H. Nishio, K. Higashi, H. Inoue, Mater. Trans. 51 (2010) 749–755.
[39] Y. Uematsu, K. Tokaji, M. Matsumoto, Mater. Sci. Eng. A 517 (2009) 138–145.
[40] T. Homma, N. Kunito, S. Kamado, Scripta Mater. 61 (2009) 644–647.
[41] S.H. Kim, W.K. Jo, W.H. Hong, W. Kim, J. Yoon, S.H. Park, Mater. Sci. Eng. A 702 (2017) 1–9.
[42] G. Garcés, E. Oñorbe, W. Gan, K. Máthis, D. Tolnai, K. Horváthd, P. Pérez, P. Adeva, Mater. Char. 126 (2017) 116–124.
[43] J. Bohlen, P. Dobroň, J. Swiostek, D. Letzig, F. Chmelík, P. Lukáč, K.U. Kainer, Mater. Sci. Eng. A 462 (2007) 302–306.
[44] J. Bohlen, P. Dobron, E.M. Garcia, F. Chmelík, P. Lukáč, D. Letzig, K.U. Kainer, Adv. Eng. Mater. 8 (2006) 422–427.
[45] M.R. Barnett, Scripta Mater. 59 (2008) 696–698.
[46] G. Gottstein, L.S. Shvindlerman, Grain Boundary Migration in Metals: Thermodynamics, Kinetics, Applications, second ed., CRC Press, 2011 Meter. Sci. Tech.
[47] G.E. Dieter, Mechanical Metallurgy, SI Metric Edition, London, 1988.
[48] I. Basu, T. Al-Samman, G. Gottstein, Mater. Sci. Eng. A 579 (2013) 50–56.

[49] R.K. Sabat, S.K. Sahoo, Mater. Des. 116 (2017) 65–76.
[50] A. Levinson, R.K. Mishra, R.D. Doherty, S.R. Kalidindi, Acta Mater. 61 (2013) 5966–5978.
[51] P.A. Beck, P.R. Sperry, J. Appl. Phys. 21 (1950) 150–152.
[52] F.J. Humphreys, M. Hatherly, Recrystallization and Related Annealing Phenomena, second ed., Elsevier, Oxford, 2004.
[53] P.G. Partridge, Metall. Rev. 12 (1967) 169–194.
[54] S.I. Wright, M.M. Nowell, D.P. Field, Microsc. Microanal. 17 (2011) 316–329.
[55] Y.J. Kim, S.H. Kim, J.U. Lee, B.S. You, S.H. Park, Mater. Sci. Eng. A 707 (2017) 620–628.